

Received May 2, 2018, accepted May 24, 2018, date of publication May 29, 2018, date of current version June 29, 2018.

Digital Object Identifier 10.1109/ACCESS.2018.2841854

Efficient Colorful Fourier Ptychographic Microscopy Reconstruction With Wavelet Fusion

JIZHOU ZHANG¹, TINGFA XU, SINING CHEN¹, AND XING WANG

School of Optics and Photonics, Beijing Institute of Technology, Beijing 100081, China

Corresponding author: Tingfa Xu (ciom_xtf1@bit.edu.cn)

This work was supported in part by the Major Science Instrument Program of the National Natural Science Foundation of China under Grant 61527802 and in part by the General Program of the National Natural Science Foundation of China under Grant 61371132 and Grant 61471043.

ABSTRACT Fourier ptychographic microscopy (FPM) is a recently developed microscope that offers wide field, high resolution, and quantitative phase imaging. Combining the concepts of ptychography, synthetic aperture, and phase retrieval, FPM overcomes the space-bandwidth-product (SBP) limit of the optical system. In FPM, a LED array is used as the illumination module and specimen images illuminated with angular varying illuminations are captured. These images are synthesized to recover the high SBP complex field of the specimen. There have been many improvements of FPM since its appearance and FPM is of great potential in the field of hematology and pathology. However, low efficiency in capturing data, especially in the situation of capturing all three color channels, limits the application of FPM. Although spectral multiplex strategy for FPM is developed, the reconstruction quality and speed is decreased for exchanging the capture efficiency. On the other hand, the reconstruction quality of FPM is significantly degraded by the imaging noise in the dark-field images because the high-frequency information in dark-field images is of low energy and contaminated by noise. In this paper, we propose an efficient colorful FPM reconstruction method using multi-resolution wavelet color fusion. We also propose an adaptive denoising method by analyzing the noise information of the dark-frame. Both simulation and experiment results are carried out to validate our methods. Results demonstrate that the imaging noise is suppressed and the colorful reconstruction is of high efficiency and quality.

INDEX TERMS Microscopy, phase imaging, high space-bandwidth-product, dark-frame denoising, multi-resolution wavelet color fusion.

I. INTRODUCTION

Fourier ptychographic microscopy (FPM) is a recently reported wide-field, high-resolution and quantitative phase imaging microscopy which overcomes the SBP limit of a low NA objective [1]–[4]. FPM is developed from the lensless imaging method termed ptychography [5]–[7] and combines the concepts of synthetic aperture [8]–[10] and phase retrieval [11], [12]. The traditional ptychography scans the specimen with a focused beam and recovers the complex field of the specimen from the diffraction patterns with phase retrieval methods. Different from ptychography, FPM scans the specimen with angularly varying oblique plane waves provided by a LED array. When a specimen is illuminated by oblique plane waves, high frequency information of the specimen is shifted into the passband of the objective. Similar to the synthetic aperture technique, FPM collects images

containing high frequency information and stitches them together in Fourier space to enlarge the bandwidth of the optical system. To recover the phase information lost in the acquisition process, FPM also applies a phase retrieval technique.

Comparing with traditional methods, FPM offers a flexible and low-cost approach to achieve high resolution, wide field and quantitative phase imaging. Researchers have implemented various modifications on both system setup and reconstruction method to improve FPM. With phase retrieval, FPM can also recover the aberration of objective lens [13], [14], the positions of LED elements [15], [16] and the defocus distance [14], [17]. To accelerate the image capture procedure, several strategies such as multiplexing [18]–[20] and content awareness [21] are developed. To improve the reconstruction speed and robustness, optimization theories like

Gauss-Newton method [20], Wirtinger flow [22] and convex relaxation [23] are introduced into FPM. New system setups for FPM such as lensless system [24], reflective system [25], fluorescent system [26] and macroscopic system [27] are also developed. Ever since the appearance of FPM, it has been widely used in many fields such as hematology [28], pathology [29], [30] and quantitative phase imaging [31]. These modifications show the great prospect of FPM in biomedical observation and clinical diagnosis. Nevertheless, there are still some issues which hinder the application of FPM.

In one hand, FPM is of low efficiency to obtain high-resolution color image. As a phase imaging method, FPM requires coherent illuminations such as lasers and LEDs. In other words, FPM can only recover the high-resolution image of one wavelength. Typically, FPM produces colorful reconstruction by merging reconstruction results with red, green and blue light, which triples the acquisition and reconstruction time. This restricts the application of FPM in observation and diagnosis that require a color vision. To solve the aforementioned problem, the wavelength multiplexing strategy is developed which captures data of three wavelength together and separates the mixed data in reconstruction process [18], [32]. With more light energy and only one capture loop, the multiplexing strategy accelerates the acquisition process. But the mixture of the three color channel decreases the redundancy of FPM data. As a result, the reconstruction speed and quality are decreased. On the other hand, the reconstruction quality of FPM is significantly degraded by the imaging noise in the dark-field images. In the acquisition process of FPM, the high frequency information in dark-field images is of low energy and usually at the same level of noise. So that, the difficulty of suppressing noise is to maintain the useful information from the noise. One traditional noise suppression strategy is to produce a high-dynamic-range (HDR) image in each LED position using a short-exposure image and a long-exposure image [1]. The HDR method decreases the dark-field noise at the expense of increasing the capture time many-fold. Several recent researches [33], [34] have been reported to perform a better reconstruction by improving the robustness of FPM reconstruction without noise suppression.

In this paper, we focus on efficiently recovering a colorful high-resolution image which is significant in observation and diagnosis. Inspired by the application of wavelet in multi-resolution fusion and color fusion [35]–[39], we develop a colorful FPM reconstruction method with wavelet fusion termed wavelet-FPM. To use wavelet-FPM, typical low-resolution monochromatic intensity images of FPM and the corresponding low-resolution color image are captured. The FPM reconstruction is performed on the monochromatic intensity images and a particular wavelet fusion process is applied on the FPM reconstruction result to recover the high-resolution color intensity image. The wavelet-FPM combines FPM to recover the high-resolution monochromatic complex field and wavelet to perform the multi-resolution color fusion.

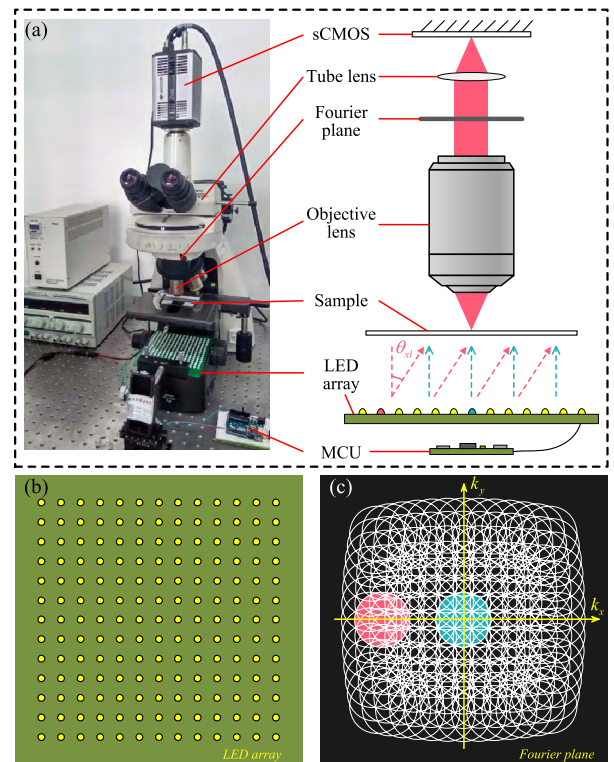


FIGURE 1. The FPM experimental system. (a) The overall appearance and diagram of FPM capture system. (b) The LED arrangement of the LED illumination module. (c) The Fourier space spectrum regions corresponding to different LED elements with the original spectrum region in blue and a shifted spectrum region in red.

Comparing with the conventional colorful FPM reconstruction methods, wavelet-FPM utilizes the low-resolution information better. Both numerical simulations and experiments on the real system are carried out to evaluate the effectiveness of wavelet-FPM. Results show that the colorful reconstruction is significantly improved comparing with conventional methods. Besides, to improve the colorful reconstruction results under noise, we propose an adaptive denoising method by using the information of noise in a dark-frame. The dark-frame method is developed based on a noise model of FPM imaging process and outperforms in results and efficiency. Experiments are also carried out to validate the effectiveness of dark-frame method.

II. PRINCIPLES AND METHODS

A. PRINCIPLE OF THE ORIGINAL FPM

The FPM system can be modified from a conventional microscopy by replacing the original illumination module with a LED array. As an example, Fig. 1 (a) shows the composition of our experimental system. The system equips a $4\times$ objective lens for optical imaging with a numerical aperture (NA) of 0.13. A scientific CMOS (sCMOS) camera with $2560 \text{ pixel} \times 2160 \text{ pixel}$ ($6.5 \text{ }\mu\text{m}$ pixel size) is used to record the intensity images. The LED array with 169 elements is placed 100 mm below the specimen for providing angle-varied illumination. All LED elements are addressable and

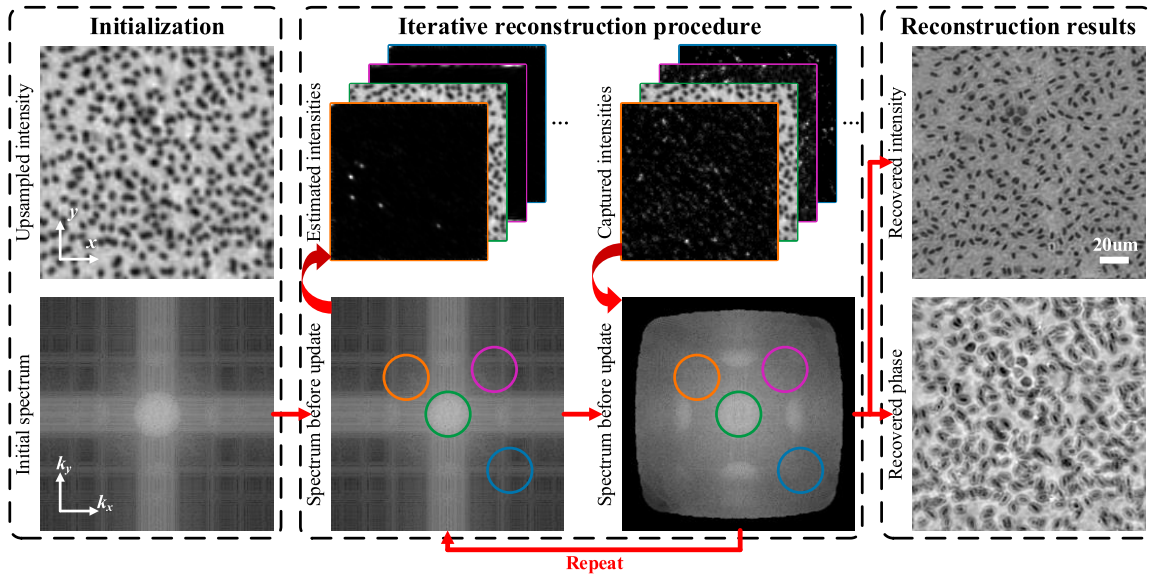


FIGURE 2. The reconstruction process of FPM. The complex field is initialized with an upsampled brightfield image and transformed into Fourier space. Then, the Fourier spectrum is iteratively updated with the captured intensity images and transformed back into real space.

programmable color pixels. In monochromatic FPM, we use only the green light (central wavelength of 505 nm) for its best reconstruction result in all three lights. In colorful FPM, we use red (629 nm), green (505 nm) and blue (460 nm) light separately or multiply. We utilize an Arduino micro-processor to control the color, sequence and exposure time of all LED elements. The LED array is accurately aligned with the brightfield localization (BFL) method [16] before acquisition.

In FPM, all samples are regarded as thin samples which modulate the amplitude and phase of incident lights. The bio-optical property of a thin sample can be represented by its transmission function $o(\mathbf{r})$, where $\mathbf{r} = (x, y)$ represents the 2D spatial coordinates in the sample plane. As the LED elements are sufficiently far from the sample stage, the illumination waves are approximately oblique plane waves. Under the oblique plane wave assumption, for the l th LED, the wave vector is

$$\mathbf{k}_l = (\sin \theta_{xl}/\lambda, \sin \theta_{yl}/\lambda) \quad (l = 1, 2, \dots, N_{LED}), \quad (1)$$

where $(\theta_{xl}, \theta_{yl})$ define the illumination angle for the l th LED and λ is the wavelength. Then the complex field entering the sample plane can be formulated as $\exp(i\mathbf{k}_l\mathbf{r})$. When the specimen is illuminated by the l th LED, the exit field passing through the sample is

$$e(\mathbf{r}) = o(\mathbf{r}) \exp(i\mathbf{k}_l\mathbf{r}). \quad (2)$$

By applying Fourier transform, the exit field is expressed as

$$\mathcal{F}\{e(\mathbf{r})\} = \mathcal{F}\{o(\mathbf{r}) \exp(i\mathbf{k}_l\mathbf{r})\} = O(\mathbf{k} - \mathbf{k}_l), \quad (3)$$

where $\mathbf{k} = (k_x, k_y)$ represents the 2D frequency coordinates. The spectrum $O(\mathbf{k} - \mathbf{k}_l)$ is also the result of spatially shifting

the sample spectrum $O(\mathbf{k})$ to be centered around \mathbf{k}_l . When passing through the objective lens, the field is low-pass filtered by the objective pupil function $P(\mathbf{k})$. The complex fields reaching the detector is

$$g_l(\mathbf{r}) = \mathcal{F}^{-1}\{P(\mathbf{k})O(\mathbf{k} - \mathbf{k}_l)\}, \quad (4)$$

which contains the high frequency information centered around \mathbf{k}_l . The low resolution intensity image captured by the image sensor can be expressed as

$$I_{lc}(\mathbf{r}) = |g_l(\mathbf{r})|^2. \quad (5)$$

Equation 1 and 2 are the forward model of FPM.

The principle of FPM reconstruction is to synthesize $g_l(\mathbf{r})$ in Fourier space and get a high-resolution complex field. However, comparing $I_{lc}(\mathbf{r})$ with $g_l(\mathbf{r})$, the phase information is lost during the imaging process. The reconstruction of FPM is to estimate the complex fields and minimize the difference between the amplitudes of estimate complex fields and the captured amplitudes. The cost function of the minimization problem is formulated as

$$\min_{O(\mathbf{k})} \epsilon = \min_{O(\mathbf{k})} \sum_l \sum_{\mathbf{r}} |I_{lc}(\mathbf{r}) - |g_{le}(\mathbf{r})|^2|^2, \quad (6)$$

where $g_{le}(\mathbf{r})$ is the estimated complex field on the image sensor. To solve the minimization problem, the phase retrieval algorithms are applied in FPM reconstruction. The most common strategy is to replace the amplitudes of estimated images with the amplitudes of captured images, known as the Alternate Projection (AP) strategy, which can be formulated as

$$g_{le}(\mathbf{r}) = \mathcal{F}^{-1}\{P(\mathbf{k})O_e(\mathbf{k} - \mathbf{k}_l)\}, \quad (7)$$

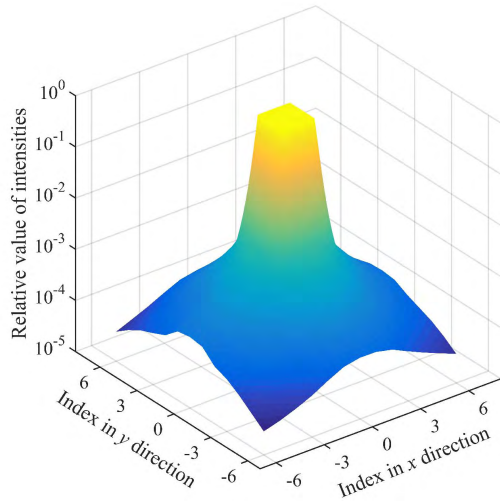


FIGURE 3. The relative values of intensities corresponding to different LEDs.

$$O_l(\mathbf{k}) = P^*(\mathbf{k}) \mathcal{F} \left\{ \frac{\sqrt{I_{lc}}(\mathbf{r})}{|g_{le}(\mathbf{r})|} g_{le}(\mathbf{r}) \right\}, \quad (8)$$

$$O_e(\mathbf{k}) = \sum_l O_l(\mathbf{k} + \mathbf{k}_l), \quad (9)$$

where $O_l(\mathbf{k})$ is the updated sub-spectrum and $O_e(\mathbf{k})$ is the whole spectrum. Equation 7 to 9 are repeated until the estimated spectrum converges and the iteration starts from an intensity-only guess of $g_{le}(\mathbf{r})$. At last, by transforming the spectrum back to the spatial domain, the high-resolution intensity and phase are extracted. The detailed iterative reconstruction process of FPM is shown in Fig. 2.

B. NOISE SUPPRESSION WITH DARK-FRAME ADAPTIVE THRESHOLD

According to the forward model of FPM, the image sensor receives the complex fields passing through the objective lens and turns the intensities of complex fields into analog electronic signals. Then, the analog electronic signals are converted into digital signals which can be easily stored and processed by a computer. However, the digital signals are contaminated by quantum noise, thermal noise, low-frequency noise and so on. As shown in Fig. 3, the intensities corresponding to edge LED positions are about 10^{-4} to 10^{-5} of the intensity corresponding to the central LED. Besides, the dynamic range of most scientific camera is not larger than 10^5 . Therefore, when the sample is illuminated with rather oblique plane waves, the intensities are of low energy and the influence of noise is non-negligible. The imaging noise in dark-field images must be suppressed or the FPM reconstruction will collapse. Traditionally, the noise is suppressed with HDR imaging or experience threshold. The HDR method improves the signal-noise ratio but slows down the capture process seriously. The experience threshold method faces difficulties in balancing the noise suppressing effect and maintaining low-energy information. We present

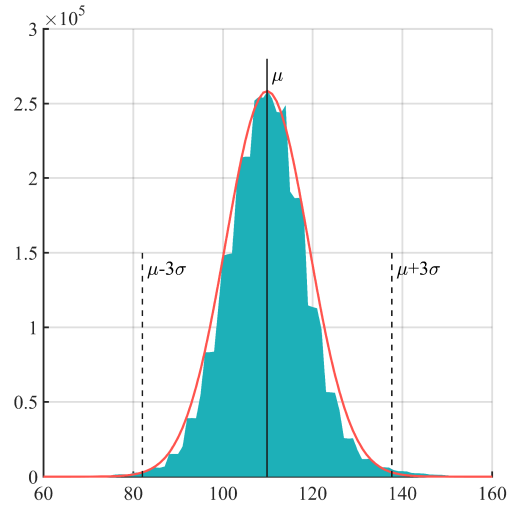


FIGURE 4. The histogram of a dark frame and the Gaussian distribution with the expectation of μ and the standard deviation of σ .

a noise model in this section to analyze the relationship between signal and noise and suppress noise according to its statistical properties.

Specifically, the intensities of FPM raw images can be divided into three parts,

$$I_{lc} = I_{li} + I_{lp} + I_{ls}. \quad (10)$$

First, I_{li} is the intensity of the ideal complex field reaching the sensor, as described in the first section. In most angles, I_{li} accounts for the main part of I_{lc} . Second, the parasitic light and dark current in the surrounding environment add extra response I_{lp} to the sensor. I_{lp} is much larger than the last factor and even larger than I_{li} in vary large angles, but it is uniform and easy to measure. The last part I_{ls} is the stochastic response of quantum noise and other stochastic noise that fits the Gaussian distribution.

To eliminate I_{lp} and I_{ls} , we capture a dark frame I_{0c} with no LED on and calculate the mean μ and standard deviation σ of I_{0c} . As shown in Fig. 4, the blue graph shows the histogram of a dark frame in our experiment and the red curve shows the Gaussian distribution with expectation of μ and standard deviation of σ . The conformance of histogram and the estimate distribution indicates the feasibility of obtaining statistical information of noise with the dark frame. According to the properties of three kinds of noise, I_{0c} contains only I_{lp} and I_{ls} . Value μ is the estimate of I_{lp} and 0 mean Gaussian distribution with standard deviation of σ is the estimate of I_{ls} standard deviation. With the 3σ principle, I_{lp} and I_{ls} can be eliminated from all intensity images by setting up an adaptive threshold

$$th = \mu + 3\sigma. \quad (11)$$

and suppress the signal response under th ,

$$I'_{lc} = I_{lc} - th. \quad (12)$$

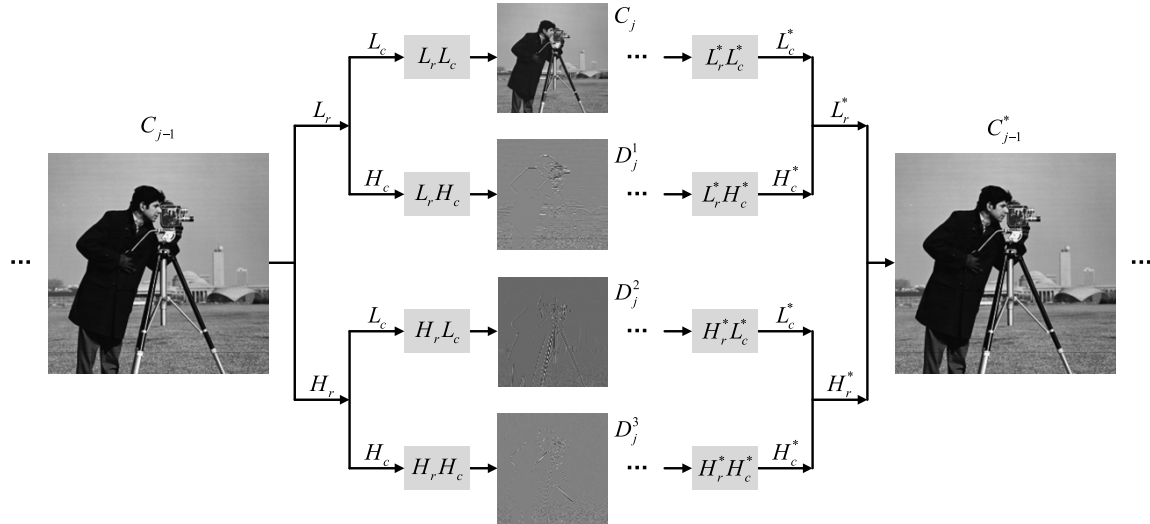


FIGURE 5. 2-D wavelet decomposition and synthesis of an image. Credits to copyright-holder of “cameraman” image: the Massachusetts Institute of Technology.

C. PRINCIPLE OF EFFICIENT COLORFUL FPM RECONSTRUCTION WITH WAVELET FUSION

As a phase imaging method, FPM requires monochromatic coherent light sources to illuminate the sample from different angles. Therefore, only the high-resolution complex field of one wavelength can be recovered with FPM reconstruction. In the conventional implementation of FPM, a colorful reconstruction is obtained by merging reconstruction results with red, green and blue light. This is the most straightforward strategy for colorful FPM reconstruction, but it triples the capture time and reconstruction time of FPM. To improve the efficiency of colorful FPM reconstruction, the wavelength multiplexing strategy is developed which captures data of three wavelength together and separates the mixed data in reconstruction process [18], [32]. Although the wavelength multiplexing strategy greatly accelerates the acquisition process, it decreases the reconstruction speed and quality. In this section, we present an efficient colorful FPM reconstruction strategy with wavelet multi-resolution color fusion, termed wavelet-FPM. Our method well balances the time consumption and reconstruction quality.

The 2-D wavelet decomposition consists of filtering and down-sampling using the 1-D low-pass filter L and high-pass filter H to each row and column of an image. Assuming C_{j-1} is the approximation of the original image C_0 and level 2^{j-1} , the 2-D wavelet decomposition in level 2^j is expressed as

$$\begin{cases} C_j = L_r L_c C_{j-1} \\ D_j^1 = L_r H_c C_{j-1} \\ D_j^2 = H_r L_c C_{j-1} \\ D_j^3 = H_r H_c C_{j-1}, \end{cases} \quad (13)$$

where the subscript r and c represent the row and column of the image. The sub-image C_j reflects the low-frequency characteristics of the original image, while D_j^1 , D_j^2 and D_j^3 reflect the high-frequency characteristics of the original image, corresponding to horizontal, vertical and diagonal directions respectively. The 2-D wavelet synthesis operation consists of up-sampling and filtering using the 1-D low-pass filter L^* and high-pass filter H^* , formulated as

$$C_{j-1}^* = L_r^* L_c^* C_j + L_r^* H_c^* D_j^1 + H_r^* L_c^* D_j^2 + H_r^* H_c^* D_j^3. \quad (14)$$

The 2-D wavelet decomposition and synthesis process of an image is shown in Fig. 5. The stepwise wavelet decomposition results of the image make up the decomposition coefficients.

By fusing the decomposition coefficients and reversely transforming the coefficients, two images of different types can be fused together and the information from two images is synthesized together. The colorful FPM reconstruction can be reached by fusing the monochromatic high-resolution reconstruction and the low-resolution color image. As a multi-resolution color fusion, the high-resolution (HR) grayscale image should be expanded to three channels and the low-resolution (LR) color image should be upsampled to the same size of high-resolution grayscale image. The fusion process is shown in Fig. 6 where the high-resolution image is captured with a $20\times$ lens and the low-resolution images is downsampled $10\times$. As shown in Fig. 6, the color and resolution are nearly the same as the groundtruth of high-resolution color image. The key points of image fusion with 2-D wavelet lie in selecting wavelet bases and fusion strategies. We design a multi-scale fusion strategy according to the properties of two image sources, termed piecewise linear strategy (PWL),

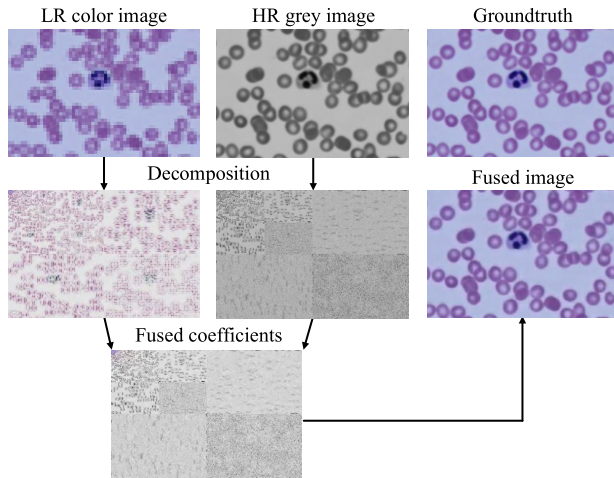


FIGURE 6. Wavelet multi-resolution color fusion of a low-resolution image and a high-resolution image.

formulated as

$$E_f = \sum_{i=1}^n [\alpha_i E_{lc} + (1 - \alpha_i) E_{hg}], \quad (15)$$

$$\alpha_i = \begin{cases} 0, & 0 < i \leq m \\ \frac{x - m}{n - m}, & m < i \leq n, \end{cases} \quad (16)$$

where E_{lc} , E_{hg} and E_f represents the decomposition coefficients of low-resolution image, high-resolution image and the fused image. α_i is the fusion weights where m is adjustable according to the resolution difference between two images. The comparison of fusion results with different wavelet bases and fusion strategies are detailed in section 3. The principle of our colorful FPM reconstruction is to fuse the FPM reconstruction in one wavelength and the low-resolution color image together. With only one reconstruction, our method achieves a state of art colorful reconstruction result while maintaining short time consumption.

III. SIMULATION AND EXPERIMENT RESULTS

A. THE EFFECTIVENESS OF DENOISING METHODS WITH ADAPTIVE THRESHOLD

The denoising process of FPM is to eliminate the noise from captured raw data while maintaining high-frequency information. A good denoising method not only improves the reconstruction results but also shortens the capture and reconstruction process. With these principles, we validate the performance of dark-frame adaptive threshold method by comparing with two conventional denoising methods. The first is the HDR imaging method and the second is the experience threshold method. As the types and levels of different imaging noises cannot be perfectly simulated, the comparisons are carried out directly on real data. The raw data is 169 images of 100 pixel \times 100 pixel human blood smear section with exposure time of 20 ms. A dark-frame with the same exposure time is captured to use the dark-frame adaptive

	Spectrum	Intensity	Phase
HDR			
Low threshold			
High threshold			
Dark-frame			

FIGURE 7. Reconstruction results comparison of three denoising methods.

TABLE 1. Experimental parameters of three denoising methods.

	HDR	threshold	dark-frame
Image number	169*6	169	169+1
Exposure time	169*630 ms	169*20 ms	(169+1)*20 ms
Processing time	0.1054 s	0.0207 s	0.0633 s

threshold method. Intensity images with 10 ms, 40 ms, 80 ms, 160 ms and 320 ms exposure time are also captured to make the HDR images. The parameters of our system are as stated in the very beginning of section II.

The reconstruction results with different denoising methods are shown in Fig. 7 and some parameters of three methods shown in Table 1. As the results shown in row 1, the reconstruction results with HDR imaging method is not very well and consumes too much time to capture images with different exposure time. As the results of low threshold and high threshold shown in row 2 and 3, experience threshold method has difficulty in finding the proper threshold. The denoising is poor when the threshold is too low and the high-frequency information is lost when the threshold is too high. With the dark-frame method, a good denoising result is achieved and high-frequency information is kept as much as possible.

B. THE COMPARISON OF DIFFERENT WAVELET BASES AND FUSION STRATEGIES

Our colorful FPM reconstruction method is actually a multi-resolution color wavelet fusion process. As illustrated in section 2, wavelet bases and fusion strategies are the key factors that affect the fusion results. In this section, we test the combination of different wavelet bases and fusion strategies.

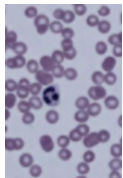
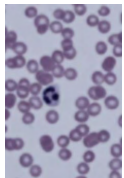
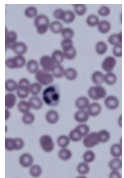
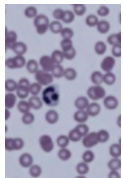
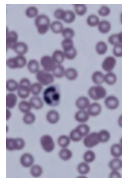
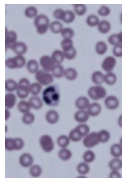
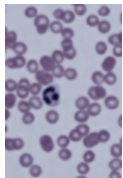
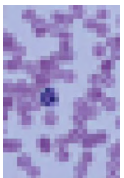







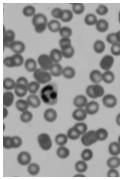







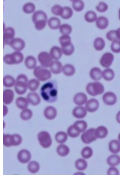
	db42	coif4	fk22	sym45	dmey	bior6.8	rbio6.8	
Averaging	 0.06250	 0.06252	 0.06252	 0.06242	 0.06252	 0.06252	 0.06252	 LR color image
Approximations and details	 0.04942	 0.04957	 0.05009	 0.04907	 0.04942	 0.04976	 0.04959	 HR gray image
PWL	 0.02565	 0.02580	 0.02596	 0.02559	 0.02599	 0.02691	 0.02590	 Groundtruth

FIGURE 8. Comparison of the multi-resolution color fusion results with 7 wavelet bases and 3 fusion strategies.

The wavelet families analyzed are Daubechies (db N , $N = 1 \dots 45$), Coiflets (coif N , $N = 1 \dots 5$), Fejer-Korovkin filters (fk N , $N = 4, 6, 8, 14, 18, 22$), Symlets (sym N , $N = 2 \dots 45$), Discrete Meyer, Biorthogonal (bior(\tilde{N} , N), (\tilde{N} , N) = (1, 1), (1,3), (1,5), (2,2), (2,4), (2,6), (2,8), (3,1), (3,3), (3,5), (3,7), (3,9), (4,4), (5,5), (6,8)), Reverse Biorthogonal (rbior(\tilde{N} , N) with (\tilde{N} , N) same as bior). We firstly select the member of each family with the best result and this member is used as the representative for this family so that it can be compared with other wavelets families. We test three coefficients fusion strategies. The first is the averaging method which takes the mean value of coefficients in each level. The second is the approximations and details method which combines the low-frequency coefficients of the low-resolution color image and high-frequency coefficients of the high-resolution grayscale image. The last is our method presented in section 2 which linearly weights the low-frequency coefficients and high-frequency coefficients according to the level.

The fusion process is the same as Fig. 6 which combines a low-resolution color image and a high-resolution grayscale image. The fusion results with 7 wavelet families and three fusion strategies are shown in Fig. 8. The corresponding root-mean-squared errors (RMSE) between fusion results and groundtruth are also shown in Fig. 8. For ease of type-setting, we rotate all images 90 degrees counterclockwise. As shown in Fig. 8, the PWL strategy achieves better results comparing with the other two strategies. Among all wavelet bases we tested, the sym40 achieves the best results and the db42 achieves the suboptimal results. Considering that sym40 consumes much more calculation, we choose db42 as our wavelet basis in wavelet-FPM.

C. THE COMPARISON OF DIFFERENT COLORFUL FPM RECONSTRUCTION METHOD

To evaluate the effectiveness of wavelet-FPM, both numerical simulations and experiments on the real system are carried out. We compare the reconstruction results of wavelet-FPM with two colorful FPM reconstruction methods. The first is combining the separate reconstruction results under red, green and blue light, called separate-FPM for short. The second is recovering red, green and blue spectrum from trichromatic white light data with wavelength multiplexing strategy, called multiplex-FPM for short.

In the numerical simulations, we use a true color image to simulate the intensity of sample and a grayscale image as the spatial phase. Low-resolution intensity images corresponding to red, green, blue and trichromatic white light are simulated with the forward model of FPM. The trichromatic white light intensities are the linear addition of red, green and blue light intensities. Colorful FPM reconstructions of separate-FPM, multiplex-FPM and wavelet-FPM are carried out using simulated intensities. The performances of three methods are shown in Fig. 9, where Fig. 9 (a), (b) show the RMSEs of recovered intensities and phases and Fig. 9 (c) shows the reconstruction results and specific RMSEs. As shown in Fig. 9, both separate-FPM and wavelet-FPM methods converge faster than the multiplex-FPM method and achieve good results. The multiplex-FPM reconstruction results of three wavelengths all contain obvious errors. Among all three methods, the wavelet-FPM achieves the lowest reconstruction error.

We also validate the reconstruction results with human blood smear images captured on a real system. Low-resolution intensity images corresponding to red, green,

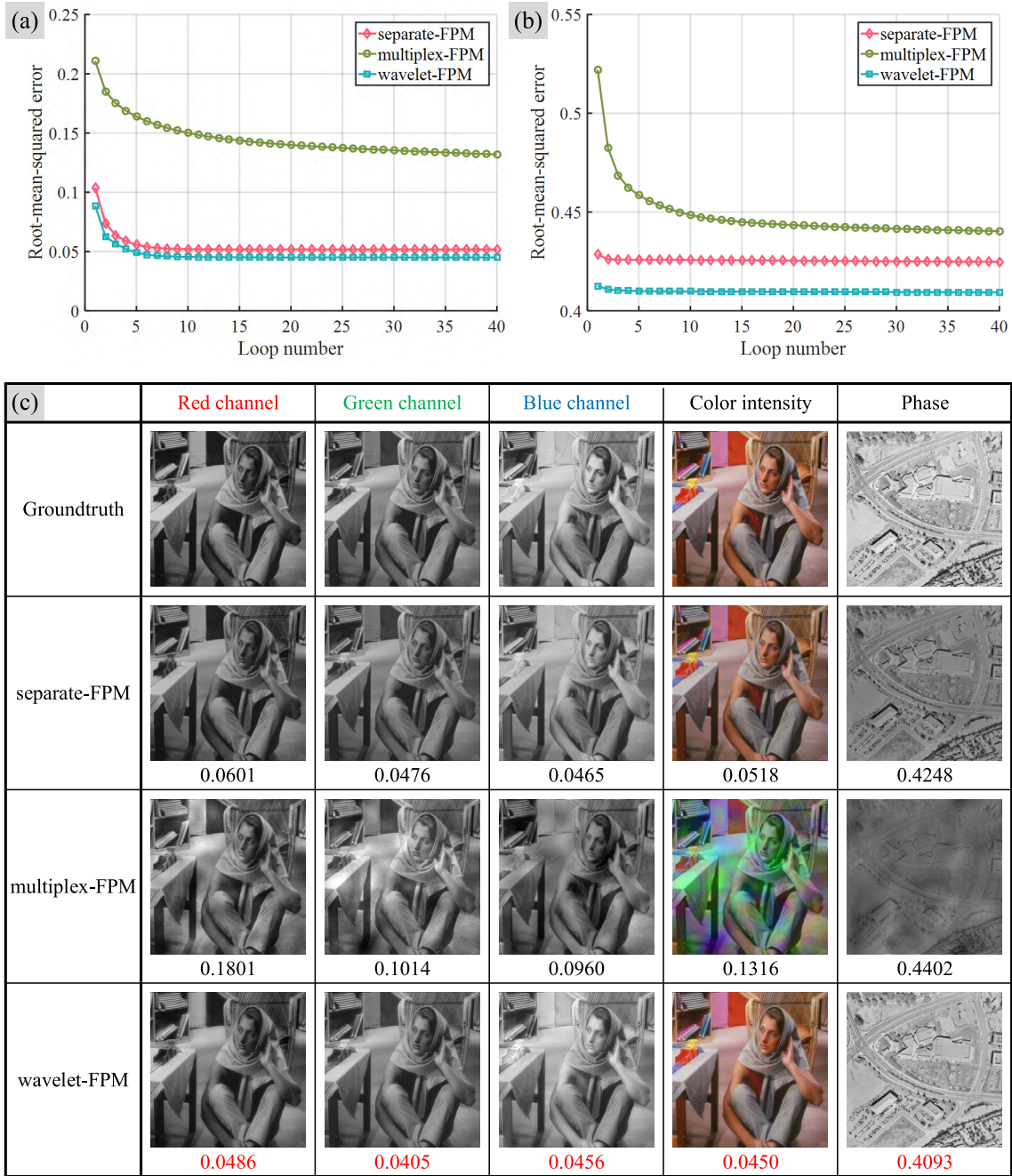


FIGURE 9. Reconstruction performance of three methods on simulate data. (a) RMSE curves of color intensity reconstruction results. (b) RMSE curves of phase reconstruction results. (c) Reconstruction results of color intensity and phase with corresponding RMSEs. Credits to copyright-holder of “barbara” image: the University of California.

blue and trichromatic white light are captured. Since the camera in our system is monochrome, the color image is obtained by merging the red, green and blue channel intensity. The color image captured under 20× magnification is also captured for comparison. Colorful FPM reconstructions of separate-FPM, multiplex-FPM and wavelet-FPM are carried out with the captured intensities. All raw images are preprocessed with dark-frame denoising method before

FPM reconstruction. The reconstruction results are shown in Fig. 10 and detailed experimental parameters are listed in Table 2. It is easy to tell that both separate-FPM and wavelet-FPM methods achieve rather good reconstruction results and converge fast. The results of these two methods are very close to the high-resolution groundtruth. The reconstruction errors in all three color channels and colorful reconstruction of multiplex-FPM are non-negligible. Among all three

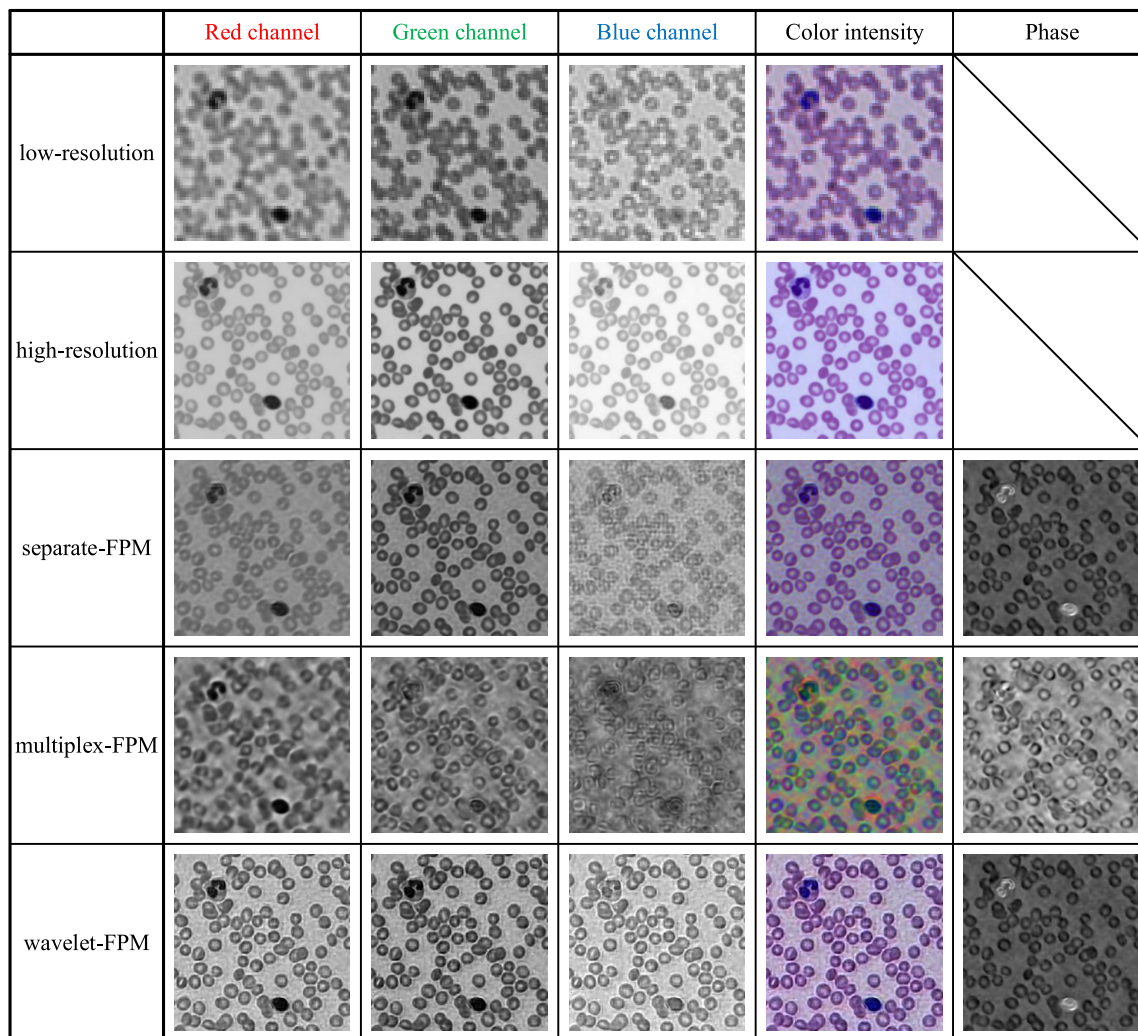


FIGURE 10. Reconstruction performance of three methods on human blood smear images.

TABLE 2. Experimental parameters of three colorful FPM reconstruction methods.

	seperate-FPM	multiplex-FPM	wavelet-FPM
Image number	169*3	169	169+3
Exposure time	169*3*30 ms	169*10 ms	(169+3)*30ms
Loop number	16	50	16
Processing time	17.6887 s	61.6940 s	7.0991 s

methods, the wavelet-FPM achieves the best reconstruction result and the least time consumption.

IV. CONCLUSION AND FUTURE WORK

In this paper, we process a colorful FPM reconstruction method termed wavelet-FPM to perform colorful reconstruction more effectively. The basic idea of wavelet-FPM is to fuse a low-resolution color intensity image and the high-resolution FPM reconstruction result of monochromatic intensities. To use wavelet-FPM, only one more low-resolution color image is needed which saves time consumption of capture process. Simulations are performed to

select the most effective wavelet bases and fusion strategies. Both simulations and experiments are performed to validate the effectiveness of wavelet-FPM. Results show that wavelet-FPM achieves better result and speed comparing with conventional methods. To improve the reconstruction results under noise, we develop a noise model and a denoising method to eliminate noise from captured raw data. Our denoising method, termed dark-frame method, use the statistical information of noise in a captured dark-frame and suppress noise under an adaptive threshold. Experiment results show that the reconstruction is improved with dark-frame method in result and speed comparing with conventional methods. The wavelet-FPM methods performs well together with the dark-frame denoising method.

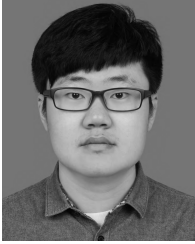
In the experiments of wavelet-FPM, we notice the great use of wavelets in FPM reconstruction. It is possible to use wavelet in more aspects of FPM. We think, the wavelet transform is able to replace the Fourier transform in FPM and makes a better use of the raw data of FPM. This can be a future work for us.

ACKNOWLEDGMENT

The authors wish to thank the anonymous reviewers for their valuable suggestions.

REFERENCES

- [1] G. Zheng, R. Horstmeyer, and C. Yang, "Wide-field, high-resolution Fourier ptychographic microscopy," *Nature Photon.*, vol. 7, no. 9, pp. 739–745, Jul. 2013. [Online]. Available: <http://www.nature.com/doi/10.1038/nphoton.2013.187>
- [2] G. Zheng, "Breakthroughs in photonics 2013: Fourier ptychographic imaging," *IEEE Photon. J.*, vol. 6, no. 2, Apr. 2014, Art. no. 0701207.
- [3] X. Ou, R. Horstmeyer, G. Zheng, and C. Yang, "High numerical aperture Fourier ptychography: Principle, implementation and characterization," *Opt. Express*, vol. 23, no. 3, pp. 3472–3491, 2015. [Online]. Available: <https://www.osapublishing.org/abstract.cfm?URI=oe-23-3-3472>
- [4] K. Guo, S. Dong, and G. Zheng, "Fourier ptychography for bright-field, phase, darkfield, reflective, multi-slice, and fluorescence imaging," *IEEE J. Sel. Topics Quantum Electron.*, vol. 22, no. 4, Jul./Aug. 2016, Art. no. 6802712.
- [5] J. M. Rodenburg and R. H. T. Bates, "The theory of super-resolution electron microscopy via Wigner-distribution deconvolution," *Philos. Trans. Roy. Soc. London A, Math. Phys. Sci.*, vol. 339, no. 1655, pp. 521–553, 1992. [Online]. Available: <http://rsta.royalsocietypublishing.org/cgi/doi/10.1098/rsta.1992.0050>
- [6] H. M. L. Faulkner and J. M. Rodenburg, "Movable aperture lensless transmission microscopy: A novel phase retrieval algorithm," *Phys. Rev. Lett.*, vol. 93, no. 2, p. 023903, 2004.
- [7] J. M. Rodenburg et al., "Hard-X-ray lensless imaging of extended objects," *Phys. Rev. Lett.*, vol. 98, no. 3, p. 034801, 2007.
- [8] T. M. Turpin, L. H. Gesell, J. Lapidés, and C. H. Price, "Theory of the synthetic aperture microscope," *Proc. SPIE*, vol. 2566, pp. 230–240, Aug. 1995.
- [9] V. Mico, Z. Zalevsky, and P. García-Martínez, and J. García, "Synthetic aperture superresolution with multiple off-axis holograms," *J. Opt. Soc. Amer. A, Opt. Image Sci.*, vol. 23, no. 12, pp. 3162–3170, 2006. [Online]. Available: <https://www.osapublishing.org/abstract.cfm?URI=josaa-23-12-3162>
- [10] T. R. Hillman, T. Gutzler, S. A. Alexandrov, and D. D. Sampson, "High-resolution, wide-field object reconstruction with synthetic aperture Fourier holographic optical microscopy," *Opt. Express*, vol. 17, no. 10, pp. 7873–7892, 2009. [Online]. Available: <https://www.osapublishing.org/abstract.cfm?URI=oe-17-10-7873>
- [11] J. R. Fienup, "Phase retrieval algorithms: A comparison," *Appl. Opt.*, vol. 21, no. 15, pp. 2758–2769, 1982. [Online]. Available: <https://www.osapublishing.org/abstract.cfm?URI=ao-21-15-2758>
- [12] A. M. Maiden and J. M. Rodenburg, "An improved ptychographical phase retrieval algorithm for diffractive imaging," *Ultramicroscopy*, vol. 109, no. 10, pp. 1256–1262, 2009. [Online]. Available: <http://dx.doi.org/10.1016/j.ultramic.2009.05.012>
- [13] X. Ou, G. Zheng, and C. Yang, "Embedded pupil function recovery for Fourier ptychographic microscopy," *Opt. Express*, vol. 22, no. 5, pp. 4960–4972, 2014. [Online]. Available: <https://www.osapublishing.org/oe/abstract.cfm?uri=oe-22-5-4960>
- [14] Z. Bian, S. Dong, and G. Zheng, "Adaptive system correction for robust Fourier ptychographic imaging," *Opt. Express*, vol. 21, no. 26, pp. 32400–32410, 2013. [Online]. Available: <https://www.osapublishing.org/oe/abstract.cfm?uri=oe-21-26-32400>
- [15] J. Sun, Q. Chen, Y. Zhang, and C. Zuo, "Efficient positional misalignment correction method for Fourier ptychographic microscopy," *Biomed. Opt. Express*, vol. 7, no. 4, pp. 1336–1350, Apr. 2016. [Online]. Available: <https://www.osapublishing.org/abstract.cfm?URI=boe-7-4-1336>
- [16] J. Zhang, T. Xu, J. Liu, S. Chen, and X. Wang, "Precise brightfield localization alignment for Fourier ptychographic microscopy," *IEEE Photon. J.*, vol. 10, no. 1, Feb. 2018, Art. no. 6900113. [Online]. Available: <http://ieeexplore.ieee.org/document/8166728/>
- [17] L. Tian and L. Waller, "3D intensity and phase imaging from light field measurements in an LED array microscope," *Optica*, vol. 2, no. 2, pp. 104–111, 2015. [Online]. Available: <https://www.osapublishing.org/abstract.cfm?URI=optica-2-2-104>
- [18] S. Dong, R. Shiradkar, P. Nanda, and G. Zheng, "Spectral multiplexing and coherent-state decomposition in Fourier ptychographic imaging," *Biomed. Opt. Express*, vol. 5, no. 6, pp. 1757–1767, 2014. [Online]. Available: <https://www.osapublishing.org/boe/abstract.cfm?uri=boe-5-6-1757>
- [19] J. Sun et al., "Coded multi-angular illumination for Fourier ptychography based on Hadamard codes," *Proc. SPIE*, vol. 9524, p. 95242C, Jul. 2015.
- [20] L. Tian, X. Li, K. Ramchandran, and L. Waller, "Multiplexed coded illumination for Fourier ptychography with an LED array microscope," *Biomed. Opt. Express*, vol. 5, no. 7, pp. 2376–2389, 2014. [Online]. Available: <https://www.osapublishing.org/boe/abstract.cfm?uri=boe-5-7-2376>
- [21] L. Bian, J. Suo, G. Situ, G. Zheng, F. Chen, and Q. Dai, "Content adaptive illumination for Fourier ptychography," *Opt. Lett.*, vol. 39, no. 2, pp. 6648–6651, 2014. [Online]. Available: <https://www.osapublishing.org/abstract.cfm?URI=ol-39-23-6648>
- [22] L. Bian, J. Suo, G. Zheng, K. Guo, F. Chen, and Q. Dai, "Fourier ptychographic reconstruction using Wirtinger flow optimization," *Opt. Express*, vol. 23, no. 4, pp. 4856–4866, 2015. [Online]. Available: <https://www.osapublishing.org/abstract.cfm?URI=oe-23-4-4856>
- [23] R. Horstmeyer, R. Y. Chen, X. Ou, B. Ames, J. A. Tropp, and C. Yang, "Solving ptychography with a convex relaxation," *New J. Phys.*, vol. 17, no. 5, p. 053044, 2015. [Online]. Available: <http://dx.doi.org/10.1088/1367-2630/17/5/053044>
- [24] W. Luo, A. Greenbaum, Y. Zhang, and A. Ozcan, "Synthetic aperture-based on-chip microscopy," *Light, Sci. Appl.*, vol. 4, no. 3, p. e261, 2015. [Online]. Available: <http://www.nature.com/doi/10.1038/lsa.2015.34>
- [25] S. Pacheco, G. Zheng, and R. Liang, "Reflective Fourier ptychography," *J. Biomed. Opt.*, vol. 21, no. 2, p. 026010, 2016.
- [26] S. Dong, P. Nanda, R. Shiradkar, K. Guo, and G. Zheng, "High-resolution fluorescence imaging via pattern-illuminated Fourier ptychography," *Opt. Express*, vol. 22, no. 17, pp. 20856–20870, 2014. [Online]. Available: <https://www.osapublishing.org/oe/abstract.cfm?uri=oe-22-17-20856>
- [27] S. Dong et al., "Aperture-scanning Fourier ptychography for 3D refocusing and super-resolution macroscopic imaging," *Opt. Express*, vol. 22, no. 11, pp. 13586–13599, 2014. [Online]. Available: <https://www.osapublishing.org/abstract.cfm?URI=oe-22-11-13586>
- [28] J. Chung, X. Ou, R. P. Kulkarni, and C. Yang, "Counting white blood cells from a blood smear using Fourier ptychographic microscopy," *PLoS ONE*, vol. 10, no. 7, p. e0133489, 2015.
- [29] R. Horstmeyer, X. Ou, G. Zheng, P. Willems, and C. Yang, "Digital pathology with Fourier ptychography," *Comput. Med. Imag. Graph.*, vol. 42, pp. 38–43, Jun. 2015. [Online]. Available: <http://dx.doi.org/10.1016/j.compmedimag.2014.11.005>
- [30] A. Williams et al., "Fourier ptychographic microscopy for filtration-based circulating tumor cell enumeration and analysis," *J. Biomed. Opt.*, vol. 19, no. 6, p. 066007, 2014.
- [31] X. Ou, R. Horstmeyer, C. Yang, and G. Zheng, "Quantitative phase imaging via Fourier ptychographic microscopy," *Opt. Lett.*, vol. 38, no. 22, pp. 4845–4848, 2013. [Online]. Available: <http://www.ncbi.nlm.nih.gov/pubmed/24322147>
- [32] Y. Zhou, J. Wu, Z. Bian, G. Zheng, and Q. Dai, "Wavelength multiplexed Fourier ptychographic microscopy," in *Proc. Conf. Comput. Opt. Sens. Imag.*, 2016, pp. 1–3.
- [33] C. Zuo, J. Sun, and Q. Chen, "Adaptive step-size strategy for noise-robust Fourier ptychographic microscopy," *Opt. Express*, vol. 24, no. 18, pp. 20724–20744, 2016. [Online]. Available: <https://www.osapublishing.org/abstract.cfm?URI=oe-24-18-20724>
- [34] Y. Fan, J. Sun, Q. Chen, M. Wang, and C. Zuo, "Adaptive denoising method for Fourier ptychographic microscopy," *Opt. Commun.*, vol. 404, pp. 23–31, Dec. 2017. [Online]. Available: <http://linkinghub.elsevier.com/retrieve/pii/S0030401817304054>
- [35] L. J. Chipman, T. M. Orr, and L. N. Graham, "Wavelets and image fusion," in *Proc. Int. Conf. Image Process.*, vol. 3, Oct. 1995, pp. 248–251.
- [36] J. Nunez, X. Otazu, O. Fors, A. Prades, V. Pala, and R. Arbiol, "Multiresolution-based image fusion with additive wavelet decomposition," *IEEE Trans. Geosci. Remote Sens.*, vol. 37, no. 3, pp. 1204–1211, May 1999.
- [37] G. Pajares and J. M. de la Cruz, "A wavelet-based image fusion tutorial," *Pattern Recognit.*, vol. 37, no. 9, pp. 1855–1872, 2004.
- [38] H. Li, B. S. Manjunath, and S. K. Mitra, "Multisensor image fusion using the wavelet transform," *Graph. Models Image Process.*, vol. 57, no. 3, pp. 235–245, 1995.
- [39] K. Amolins, Y. Zhang, and P. Dare, "Wavelet based image fusion techniques—An introduction, review and comparison," *ISPRS J. Photogramm. Remote Sens.*, vol. 62, no. 4, pp. 249–263, 2007.



JIZHOU ZHANG received the bachelor's degree from the School of Optics and Photonics, Beijing Institute of Technology, Beijing, China, in 2014, where he is currently pursuing the Ph.D. degree. His research interests include Fourier ptychographic microscopy, computational imaging, and machine learning.



SINING CHEN is currently pursuing the M.E. degree with the School of Optoelectronics, Beijing Institute of Technology, Beijing, China. Her research interests include computer imaging and Fourier ptychographic microscopy.



TINGFA XU received the Ph.D. degree from the Changchun Institute of Optics, Fine Mechanics and Physics, Changchun, China, in 2004. He is currently a Professor with the School of Optoelectronics, Beijing Institute of Technology, Beijing, China. His research interests include optoelectronic imaging and detection and hyper-spectral remote sensing image processing.



XING WANG is currently pursuing the M.E. degree with the School of Optoelectronics, Beijing Institute of Technology, Beijing, China. Her research interests include computer vision and Fourier ptychographic microscopy.

...